Lofting of low-speed ejecta produced in the DART experiment and production of a dust cloud

Gonzalo Tancredi [ID],[1]★ Po-Yen Liu,[2] Adriano Campo-Bagatin,[2,3] Fernando Moreno [ID][4] and Bruno Domínguez[1]

[1]*Departamento de Astronomía, Facultad de Ciencias, Iguá 4225, 11400 Montevideo, Uruguay*
[2]*Instituto Universitario de Física Aplicada a las Ciencias y las Tecnologías. Universidad de Alicante, San Vicent del Raspeig, E-03690 Alicante, Spain*
[3]*Departamento de Física, Ingeniería de Sistemas y Teoría de la Señal. Universidad de Alicante, San Vicent del Raspeig, E-03690 Alicante, Spain*
[4]*Instituto de Astrofísica de Andalucía, CSIC, Glorieta de la Astronomía s/n, E-18008 Granada, Spain*

ABSTRACT

NASA sent the Double Asteroid Redirection Test (DART) mission to impact Dimorphos, the satellite of the asteroid binary system (65803) Didymos. DART will release LICIACube prior to impact to obtain high-resolution post-impact images. The impact will produce a crater and a large amount of material ejected at high speed (several tens of $m\,s^{-1}$), producing an ejecta cone that will quickly disperse. We analysed an additional effect: the lofting of material at low velocity due to the generation of seismic waves that propagate inside Dimorphos, producing surface shaking far from the impact point. We divide the process into different stages: from the generation of impact-induced waves, the interaction of them with surface particles, the ejection of dust particles at velocities, and the prediction of the observability of the dust coma and trail. We anticipate the following observable effects: (i) generation of a dust cloud that will produce a hazy appearance of Dimorphos' surface, detectable by LICIACube; (ii) brightness increase of the binary system due to enhancement of the cross-section produced by the dust cloud; (iii) generation of a dust trail, similar to those observed in some Active Asteroids, which can last for several weeks after impact. Numerical prediction of the detectability of these effects depends on the amount and size distribution of ejected particles, which are largely unknown. In case these effects are observable, an inversion method can be applied to compute the amount of ejected material and its velocity distribution, and discuss the relevance of the shaking process.

Key words: waves – software: simulations – minor planets, asteroids: general – minor planets, asteroids: individual: Dimorphos.

1 INTRODUCTION

Humanity has recognized the consequences that an impact of an asteroid or comet can have on the development of life on Earth. For this reason, various strategies have been designed to deal with this threat. Among the options analysed, the deflection of the object well before impact is the most promising. One of the methodologies proposed for deflection is a kinetic impact: hitting the body with a massive object to transfer linear momentum that changes its course. The net transfer of momentum depends on many factors, like the size, internal structure, and material properties of the target, as well as the amount and velocity distribution of ejected material. To perform a real test of the kinetic impactor method, in 2021 November, NASA launched the Double Asteroid Redirection Test (DART) mission to impact Dimorphos, the satellite of asteroid (65803) Didymos. The impact experiment will occur on 2022 September 26 23:14 UT. At impact time, the DART spacecraft will have a mass of about 550 kg, and a speed of 6.6 $km\,s^{-1}$ (Rivkin et al. 2021).[1] DART will be

able to take images during the approach, and send them to Earth, up to a couple seconds before impact. 15 d prior to impact, DART will release the Italian Space Agency's (ASI) 'Cubesat' LICIACube. LICIACube will follow a similar trajectory, with a closest approach to Dimorphos 167 s after impact at a distance of 51 km.

The DART impact will likely produce a crater on Dimorphos (or, alternatively, will deform it, Raducan, Davison & Collins 2022) and a large amount of material will be ejected at high speed (several tens of $m\,s^{-1}$), producing an ejecta cone that will quickly disperse (Fahnestock et al. 2022). The ejecta cone should be observable by LICIACube in the first few seconds after impact. Additionally, during the crater formation phase, low-speed ejecta would be launched from the outer rims of the crater and the surrounding region (up to a few times the impactor size), as predicted from ejecta scaling laws based on the point-source assumption-based scaling models (Housen & Holsapple 2011). Moreover, impact generated seismic waves may propagate inside the target and reach the surface triggering motion

report on the final values of the impact parameters, like the final mass and velocity of the space probe and mass of the target. Nevertheless, two of the authors (GT and ACB) are members of the DART International Team, and the information to which they have access confirms that deviations from the assumed values are not relevant to the results of this work.

★ E-mail: gonzalo@fisica.edu.uy
[1]The manuscript was initially submitted before the impact, and it was reviewed a few days after. First, we note that the impact did occur at the expected time. At the time of revising the manuscript, there is no official

of fines that may overcome the escape velocity and produce a late trail of dust (Tancredi et al. 2012). The latter effect may take place even in the case of target deformation.

Different sets of data have been used to derive the most relevant physical and orbital parameters for the Didymos-Dimorphos systems. They are summarized in the Didymos Reference Model adopted by ESA. The mean radius of Dimorphos is $r_{Dim} = 84$ m, and the derived mass is $M_{Dim} = 4.83 \times 10^9$ kg.

Two critical speeds need to be taken into account when discussing the outcome of low-speed ejecta: (i) the escape velocity from the surface of Dimorphos: $v_{esc,Dim} \approx 0.089$ m s^{-1}; and (ii) the escape velocity from the binary system (at the distance of Dimorphos from Didymos): $v_{esc,Sys} \approx 0.24$ m s^{-1}. On one hand, if particles are launched with any outgoing speed v (positive radial component respect to the centre of mass of Dimorphos) lower than $v_{esc,Dim}$, they will fall back on Dimorphos. If outwards speed is between $v_{esc,Dim}$ and $v_{esc,Sys}$, particles will be moving in the binary system, and eventually collide with one of the two bodies. Instead, if there is enough time for solar radiation pressure (SRP) to act, small particles can be removed from the system. On the other hand, if a particle's speed is larger than $v_{esc,Sys}$, it will escape from the binary system with a velocity at infinity given (U) by: $U^2 = v^2 - v_{esc,Sys}^2$ (without taking into account the effect of SRP).

Another set of relevant parameters are the acceleration on the surface of Dimorphos due to its self-gravity: $a_{Dim} \approx 4.90 \times 10^{-5}$ m s^{-2}; and the acceleration due to Didymos gravity at the distance of Dimorphos: $a_{Sys} \approx 2.53 \times 10^{-5}$ m s^{-2}.

The goal of this work is to analyse the potential detection conditions of low-speed ejecta from the DART experiment, similarly to the ejection detected in some of the so-called Active Asteroids, or Main-Belt Comets (MBCs). In Section 1.1, we discuss some findings regarding this population that are relevant for our study.

To understand the generation of the low-speed ejecta and its detectability, we combined the analysis of the following processes, under the assumption of a gravitational aggregate structure for Dimorphos:

(i) Propagation of impact-induced seismic waves at distances far from the impact point.

(ii) The local effect of these waves into small particles located on the surface, and the ejection mechanism at speeds comparable to the escape velocity of Dimorphos and the Didymos system.

(iii) Evolution of ejected particles under the influence of SRP and the gravity field of Didymos and Dimporphos.

(iv) Prediction of the observation of such cloud of particles from LICIACube and from the Earth.

Hereby, we give detailed information on the studies involved in the processes listed above, the simulations required to get the results and the expected outcome:

(i) We model the post-impact effects into a gravitational aggregate by means of two independent discrete element method (DEM) codes, including mutual gravity among particles. The hypervelocity impact of the DART projectile is replaced by the impact of a larger, lower mass synthetic projectile, so that conservation of momentum holds and the same amount of residual kinetic energy is delivered to the target. The residual energy, going into the target once the very shattering phase is over, is estimated from laboratory experiments (Walker et al. 2013). We then compute the evolution of particles close to the surface as a function of the angular distance from the impact point (angle Impact-Centre-Surface point). Section 2 is devoted to this item.

(ii) We model the incidence of a shock from below into a surface layer of particles. Particles on the upper part of a surface layer will be lofted by a shock at its bottom. We analyse the distribution of velocity of ejected particles and compare it with the escape velocity from the Dimorphos surface ($v_{esc,Dim}$) and from the Didymos binary system at the distance of Dimorphos ($v_{esc,Sys}$). This is explained in Section 3.

(iii) We analyse the dynamical evolution of particles ejected at slow speed to obtain the velocity distribution when particles escape the binary system. When particles enter interplanetary space, they undergo SRP, therefore they are pushed away from the Sun, forming a cometary-like tail, an effect that has already been observed in several so-called Active Asteroids or MBCs (see Section 1.1).

(iv) The outcome from the previous stages can be used to generate synthetic images of the comae and the tails as seen from the Earth at different times after the impact. We also discuss the observation conditions that the LICIACube flyby could encounter.

These two last items were analysed by Moreno et al. (2022) in a companion paper. In Section 4, we highlight their main conclusions and we include some further analysis of observational consequences of the low-speed ejecta.

In Section 5, we discuss the results of the previous items, taking into account the lessons learned from the observations of Active Asteroids.

1.1 Lessons learned and to be learned from Active Asteroids

The small bodies coming to the inner region of the Solar System has been classified in two groups: asteroids and comets. They are observationally distinguished because comets present – at some part of their orbit – a coma and a tail generated after the release of gas and dust from the solid nucleus; while asteroids are inert. These differences were interpreted as a consequence of material constituents: comets have a mixture of refractory materials and ices, where the latest can sublimate due to the Sun heat; while asteroids are formed with only refractory material, as was confirmed by several space missions to such objects.

This physical distinction has led to identifying some properties in the orbital parameters phase-space that can be used to characterize those two populations. A detailed analysis of the orbital classification can be found in Tancredi (2014). Based on this kind of classification, puzzling objects are found: inactive objects with cometary-type orbits (the so-called 'Asteroids in Cometary Orbits), and asteroids that showed some kind of cometary-like activity (production of comae and tails), but they are in typical asteroidal orbits (the so-called 'Comets in Asteroidal Orbits - CAOs', or 'Active Asteroids'). Among the latter group, there are some objects that show recurrent activity events, and they were named as 'MBCs'. For a recent review on the topic, see Jewitt & Hsieh (2022).

The physical processes associated with the onset of cometary-like activity on Active Asteroids are still a matter of debate. We wish to emphasize the 'cometary-like activity' term: comet activity is driven by the sublimation of ices and the release of dust embedded in the ice. Instead, it has not been proven so far that ice sublimation has ever taken place on Active Asteroids (not even on MBCs). In fact, no gaseous species have been detected so far, only the dust in the coma and tail was observed.

Nevertheless, there is consensus among scientists working on this topic, that activity on several Active Asteroids was generated after impacts and the consequent release of large amounts of dust, as was likely the case of asteroids (596) Scheila and P/2016 G1 (Jewitt et al.

2011; Moreno et al. 2011; Hainaut et al. 2019). From the analysis of the evolution of the tail, it has been concluded that the generation of the long-lasting tails can only be explained if dust is ejected at velocities just above the escape speed of the bodies. Let's take the example of active asteroids P/2019 A4 and P/2021 A5, studied by Moreno et al. (2021). The upper limits for the sizes of these objects are: diameter $D = 0.7 - 1.0$ km for P/2019 A4, and $D = 2.4$ km for P/2021 A5; although the sizes derived from the dust-formation Monte Carlo modelling are much smaller: 100–240m (nominal value 170m) for P/2019 A4, and smaller than 500m (nominal value 150m) for P/2021 A5. The estimates of the total dust mass ejected were $(2.0 \pm 0.7) \times 10^6$ kg and $(8 \pm 2) \times 10^6$ kg for P/2019 A4 and P/2021 A5, respectively, for particle-size distributions having a maximum particle radius of 1cm. The derived ejection speeds for both objects $\sim$0.2 m s^{-1} are consistent with the escape speeds at the surface corresponding to the nuclear radii estimated from the Monte Carlo modelling.

Assuming that the ejected material was produced in a cratering event, Moreno et al. (2021) used the cratering scaling–law by Housen & Holsapple (2011) with an impact speed of 5 km s^{-1}, ejection speed of 0.23 m s^{-1}, and ejected mass of 2×10^6 kg, to estimate an impactor mass of 200 kg in the case of P/2019 A4.

In summary, the coma and long-lasting tails observed for a few months on those km-size Active Asteroids are explained by a single impact event of a few hundreds kg projectile, where a few thousands of tons of mm to cm-size dust particles are released at speeds just above the escape speed at the surface of those bodies.

Since the comae and the tails of those Active Asteroids were detected long after the generation event, it is not possible to infer the physical mechanism that produced the low-speed ejecta. We also do not know the fraction of high-speed ejecta produced at impact, because such ejecta was already dispersed at the time of the observation.

The DART experiment can be considered as the generation of an artificial Active Asteroid, with a precise impact date, impact speed, and mass of the impactor. Similar observational effects are foreseen: brightness increase of several magnitudes above the nucleus', and production of a long tail. Given that the LICIACube will monitor the impact and the outcome in the few minutes afterwards, and that there will be a large battery of ground-based and space-based telescopes monitoring the event up to several weeks later, we will have the opportunity to get insight on the generation of an Active Asteroid. The DART event will give useful information for understanding the detailed physics of this phenomena.

2 PROPAGATION OF IMPACT-INDUCED SEISMIC WAVES

2.1 DART and Dimorphos initial setup

At this initial stage, we investigate the possible reaction of Dimorphos to the DART collision, under the assumption that it is a spherical gravitational aggregate produced in the formation of the binary system (Walsh, Richardson & Michel 2008). The very internal structure of the target is unknown therefore we model the target by a multi-dispersed distribution of $\approx 100\,000$ spherical particles, with particle radii ranging from 1.0 to 2.5 m and a random packing configuration. The total mass of the particles corresponds to the mass of Dimorphos mentioned above.

We perform numerical simulations of the DART collision event on Dimorphos using two different DEM codes (Section 2.2). We neglect the presence of Didymos, since it does not affect the dynamics on

Dimorphos's particles along the small time-scale of the collision event, while the momentum and energy propagation takes place. The real DART impact will be a hyper-speed cratering event, where most of the impact kinetic energy goes into the shattering phase, which implies local vaporization, melting, rock deformation, and heat transfer. Therefore, due to the fact that DEM codes are not suitable to simulate the shattering phase itself, we instead concentrate on the effect of the collision on the part of the target not affected by such phase, once it is over. That means that the kinetic energy delivered to the rest of the body is just a small fraction of the impact energy. Therefore, our synthetic projectile needs to deliver the same nominal linear momentum to Dimorphos as the DART spacecraft will, but it only delivers to the target a small fraction of the original impact kinetic energy. According to cratering experiments (Walker et al. 2013), only a small fraction $f_{ke} \approx 0.25$ per cent of impact energy will survive as kinetic energy of the target after the shattering phase.

In order to apply this model, we replace the real DART spacecraft, with mass M and velocity V, with a synthetic projectile with the same linear momentum as DART and a kinetic energy corresponding to the small fraction surviving the impact. The real DART projectile carries a kinetic energy $E = \frac{1}{2}MV^2 = 1.2 \times 10^{10}$ J and linear momentum $P = MV = 3.6 \times 10^6$ kg.m s^{-1}. The synthetic projectile has mass m_0 and velocity v_0. After the impact, we assume that our synthetic Dimorphos will receive a residual kinetic energy of $f_{ke}E$ as a whole, and a linear momentum P. The latter includes the linear momentum P_{ej} taken away by the particles ejected and the linear momentum P_T that Dimorphos itself actually received.

However, unlike reality, our synthetic projectile will not be destroyed by the impact, it will just rebound on the synthetic Dimorphos with a given restitution coefficient ϵ (which is assumed to be 0.3, as for typical Earth rocks). Therefore, our synthetic projectile carries away a kinetic energy $E_0 = \frac{1}{2}m_0(\epsilon v_0)^2$. In addition, the initial linear momentum P_0 of our synthetic projectile must be equal to the linear momentum of Dimorphos itself (P) and the ejecta plus the linear momentum taken away by the rebound synthetic projectile ($\epsilon m_0 v_0$). The above description leads to the following equations:

$$(1 + \epsilon)m_0 v_0 = MV \tag{1}$$

$$\frac{1}{2}m_0 v_0^2 = \frac{1}{2}m_0(\epsilon v_0)^2 + f_{ke}\frac{1}{2}MV^2. \tag{2}$$

By solving such equations, we obtain the following expressions for the mass and velocity of the synthetic projectile, as a function of the parameters ϵ and f_{ke}:

$$m_0 = \frac{M}{f_{ke}}\frac{(1 - \epsilon)}{(1 + \epsilon)} \tag{3}$$

$$v_0 = \frac{f_{ke}V}{(1 - \epsilon)} \tag{4}$$

2.2 Modelling the outcome of the DART impact

To numerically simulate the effects of the DART impact event and the propagation of the induced momentum and kinetic energy waves into the interior of a synthetic Dimorphos, we used two different DEM codes:

(i) The high-performance *PKDGRAV* parallel gravitational *N*-body numerical code (Richardson et al. 2000), with an implementation of the soft-sphere DEM (*SSDEM*; Schwartz, Richardson & Michel 2012) with gravity. *SSDEM–PKDGRAV* has been extensively used in simulations of rubble-pile models of asteroids. The contact model among the particles is a linear spring-dashpot, in which the

**Table 1.** Relevant parameters for the simulated DART impact.

Mean radius of Dimorphos	84 m
Total mass of Dimorphos	4.83×10^9 kg
Particles sizes	1–2.5 m
Particle density	4156 kg m^{-3}
Projectile radius	1.485 m
Projectile mass	140 000 kg
Projectile density	10 208 kg m^{-3}
Projectile velocity	23.75 m s^{-1}
Impact point	$20°$ below equator
Projectile velocity vector	pointing radially to the centre

dashpot force is linearly proportional to the normal and tangential relative velocities. The code also takes into account tangential friction forces between contact surfaces. The resistance force acting on the surfaces of the contacting particles will also impose a torque on both particles. By integrating the force and torque, the motion of a particle can then be determined.

(ii) An extended version of the open-source DEM code *ESyS-Particle* (https://launchpad.net/esys-particle Abe, Place & Mora 2004), which includes self-gravity between particles. *ESyS-Particle* was first applied in planetary sciences by Tancredi et al. (2012), including simulations in low-gravity environments (asteroids and comets) and new models to simulate contact forces. These early simulations included only a global gravity force in one space direction. In the following articles: Frascarelli, Nesmachnow & Tancredi (2014), Rocchetti, Nesmachnow & Tancredi (2018, 2021), and Nesmachnow, Rocchetti & Tancredi (2019), the authors described a self-gravity module that applied high-performance computing techniques to enable simulations of hundred of thousands particles efficiently. Different strategies to compute long-range forces were introduced, implemented, and evaluated in realistic scenarios. This extended version of *ESyS-Particle*, which include self-gravitation, is called *ESyS-Gravity*. In *ESyS*, the user can select the contact model among different alternatives. In our simulations, we have used a linear spring-dashpot and a Hertzian–viscoelastic interaction model with friction.

We performed numerical simulations using the same initial conditions for both codes. For the nominal configuration, we assumed an efficiency factor $f_{ke} = 0.0025$ (0.25 per cent) and a restitution coefficient $\epsilon = 0.3$. Using equations (3) and (4), we computed the mass and velocity of the projectile, which are listed in Table 1. The impact occurs at a point on the surface $20°$ below the equator, and the projectile velocity vector points radially towards the centre of the target.

Input parameters related to elastic properties are different among the two codes. *PKDGRAV* uses the restitution coefficient ($\epsilon = 0.3$) and a given maximum allowed overlap during a collision ($\delta R = 3$ per cent), as well as suitable time-step and elastic constant, dependent on the system characteristics. Namely, during 3 s of simulated time, due to the high speed collision from the synthetic DART impactor, we use a short-time step of 3×10^{-5} s and a spring constant of 1.58×10^{12} kg s^{-2}. For the nominal case, in *ESyS-Gravity*, we use the linear spring-dashpot model with a spring constant of 10^9 *Pa*, a damping coefficient 10^5 (m s)$^{-1}$, and a coefficient of friction $\nu = 0.1$ (see a description of the model in Abe et al. 2004), which produces a restitution coefficient similar to the one assumed by PKDGRAV in experiments like the bouncing of two 1 *m* equal spheres. The simulations with *ESyS-Gravity* were run for 10s of simulated time, with a time-step of 10^{-4} s.
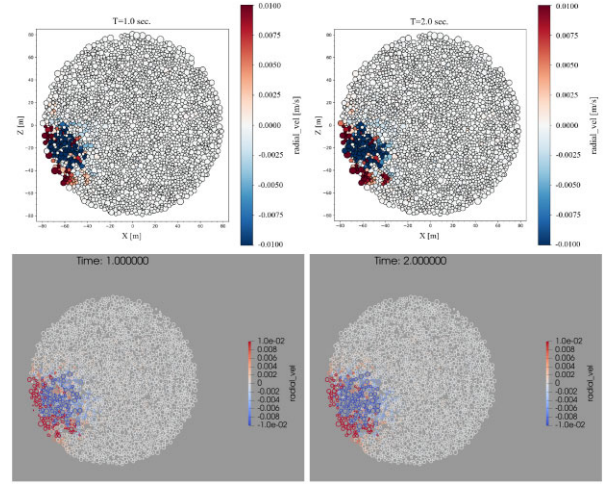
Figure 1. Snapshots of a cross-section through the centre of the target and the impact point. The upper row corresponds to simulations with *SSDEM–PKDGRAV*, and the lower row to simulations with *ESyS-Gravity*. The left-hand plots are snapshots at 1 s after impact, and the right-hand plots at 2 s. The colour bar is proportional to the value of v_{rad}, the projection of the particle's velocity vector along the radius vector of the particle. Red colour corresponds to outward velocities (positive values) and blue colour to inward velocities (negative values).

2.3 Summary of results of energy and momentum propagation

As a consequence of the propagation of the impact-induced seismic wave, there is a large scatter between the evolution of the particles on the surface and the interior.

In Fig. 1, we present snapshots at 1 and 2 s after the impact of a cross-section through the centre of the target and the impact point. The colour bar is proportional to the value of v_{rad}, the projection of the particle's velocity vector along the radius vector of the particle. Red colour corresponds to outward velocities (positive values) and blue colour to inward velocities (negative values). The upper plots correspond to simulations using *SSDEM–PKDGRAV*, while the lower ones to simulations using *ESyS-Gravity*.

We do not go into a detailed comparison of both sets of simulations, but we observe that the velocity field pattern in the interior looks very similar in both models.

Let's recall that the impact point in both models is $20°$ below the equatorial plane (lower-left part in each snapshot of Fig. 1). 2 s after impact (upper and lower-right plots), particles moving inward (blue colour scale) reached up to about half the radius of the target. We observe that the seismic wave going to the interior bounces back, and produces outward displacement on the surface and inward displacement in the interior. The range of speed values is the same in both models. The volume affected by the impact induced wave is a half sphere, centred on the impact point, with a radius approximately half the body radius. Note that particles on the surface are moving outwards (red colours).

We conclude that the results obtained with the two models are comparable. Hereafter, we will present the results using only *ESyS-Gravity*, as it can be later applied to the propagation of linear momentum and kinetic energy all the way to small particles on the surface (Section 3).

We are mainly interested in the effects on the surface particles at locations several times away from the expected crater radius.

To analyse the effects on the particles far from the impact point, we consider three vector parameters: the displacement (ΔP) with respect
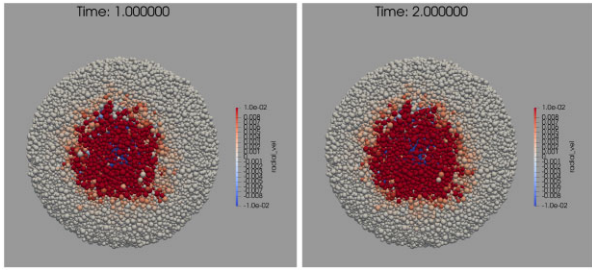
Figure 2. Snapshots at 1 and 2 s after the impact, from a viewpoint located above the impact point. The simulations were done with *ESyS-Gravity*. The colour bars are the same as the ones used in Fig. 1.

to the original position (*P*), the velocity (*v*), and the acceleration (*a*). We compute the radial projection of these vector parameters, i.e. the dot product of $\Delta P_{rad} = \Delta P \cdot P$, $v_{rad} = v \cdot P$, and $a_{rad} = a \cdot P$.

In Fig. 2, we present snapshots at 1 and 2 s after the impact, from a viewpoint located above the impact point. The colour bars are the same as the ones used in Fig. 1. Note that at distances of 30–40° from the impact point, particles are moving outward with speeds over 10^{-2} m s^{-1}.

In the supplementary material, we provide videos showing the evolution of radial velocity in the cross-section and top-view plots, up to 10 s after impact. Note that the region affected by the wave rapidly increase in the first ∼1 s, and it does not considerably increase after 2 s after impact. We estimate that the seismic wave reaches halfway to the centre (40 m depth) at ∼0.4 s after impact, which implies a wave speed of ∼100 m s^{-1}. But it requires a much longer time (>3 s) to reach the centre (80 m depth), meaning that variation of the speed is extremely non-linear. Note that the material under the surface of an agglomerated asteroid are under very low-pressure, much lower than the lowest pressure that could be attained in the lab experiment on the Earth's surface. The velocities measured in lab experiments for the lowest pressures are ∼150–200 m s^{-1} (Goddard 1990; Gallot, Tancredi & Ginares 2019). Those works also showed that the wave speed decreases with the confining pressure. These range of seismic speeds are in agreement with our estimates from the numerical simulations. However, the variation of the propagation speed of seismic waves is a problem that merited a detailed study, which is outside the scope of this work.

We focus our analysis on particles that are close to the surface. Particles that are up to 7 m below the surface are selected. The evolution of the speed for over 600 particles closer than 60° from the impact point is shown in Fig. 3. In spite of the messiness of this plot, we note that the increase in speed is a sharp step-wise function. In Fig. 4*a*, we plot the maximum outward radial velocity, and in Fig. 4*b*, the maximum outward radial acceleration, as a function of the surface angle to the impact point (up to 60°), during the simulated time. In Fig. 4*a*, the red-dotted line corresponds to the escape speed at the surface of Dimorphos ($v_{esc, Dim}$); the red-dashed line corresponds to the escape speed from the binary system at the distance of Dimorphos from Didymos ($v_{esc, Sys}$). In Fig. 4*b*, the red-dotted line corresponds to the gravity acceleration on the surface of Dimorphos (a_{Dim}); the red-dashed line corresponds to the acceleration due to gravity by Didymos at the distance from Dimorphos (a_{Sys}). From the evolution of the speed presented in Fig. 3, we note that the maximum radial velocity and acceleration for closer than 60° from the impact point are attained at less than 1 s after impact. The rise time of the velocity is computed as the time it takes to go from $v < 10^{-4}$ m s^{-1} to v
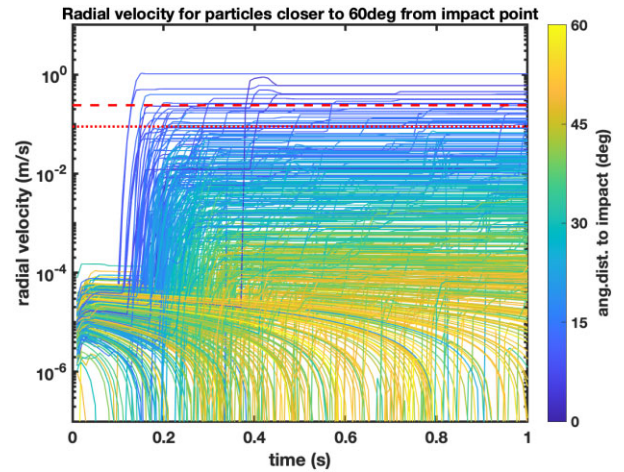

Figure 3. The evolution of the speed for over 600 particles closer than 60° from the impact point and at depth up to 7 m below the surface.
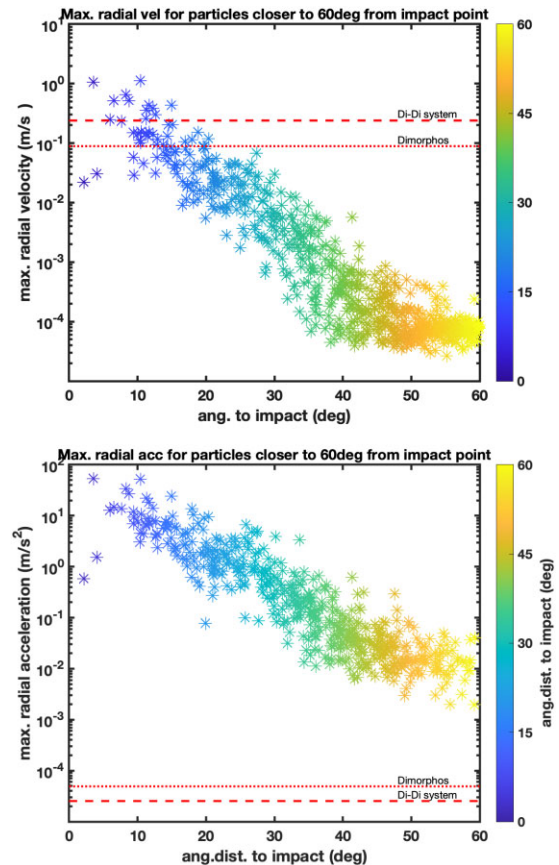

Figure 4. (a) The maximum outward radial velocity as a function of the surface angle to the impact point (up to 60°), during the simulated time. The red-dotted line corresponds to the escape speed at the surface of Dimorphos ($v_{esc, Dim}$); the red-dashed line corresponds to the escape speed from the binary system at the distance of Dimorphos from Didymos ($v_{esc, Sys}$). (b) The maximum outward radial acceleration as a function of the surface angle to the impact point (up to 60°). The red-dotted line corresponds to the gravity acceleration on the surface of Dimorphos (a_{Dim}); the red-dashed line corresponds to the acceleration due to gravity by Didymos at the distance from Dimorphos (a_{Sys}).
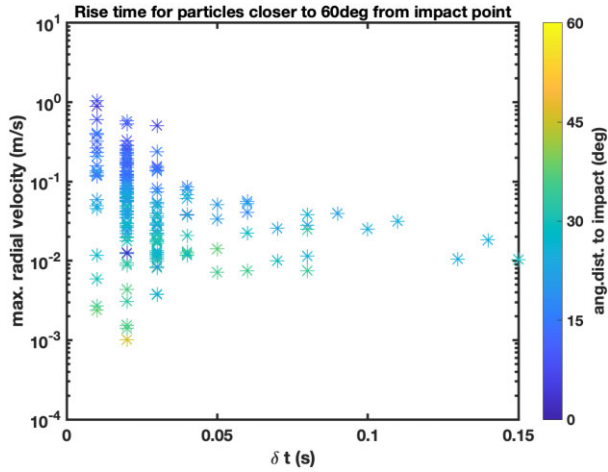
Figure 5. The rise time as a function of the maximum radial velocity. The rise time of the velocity is computed as the time it takes to go from $v < 10^{-4}$ m s^{-1} to $v > 10^{-3}$ m s^{-1}, at some moment of simulated time.
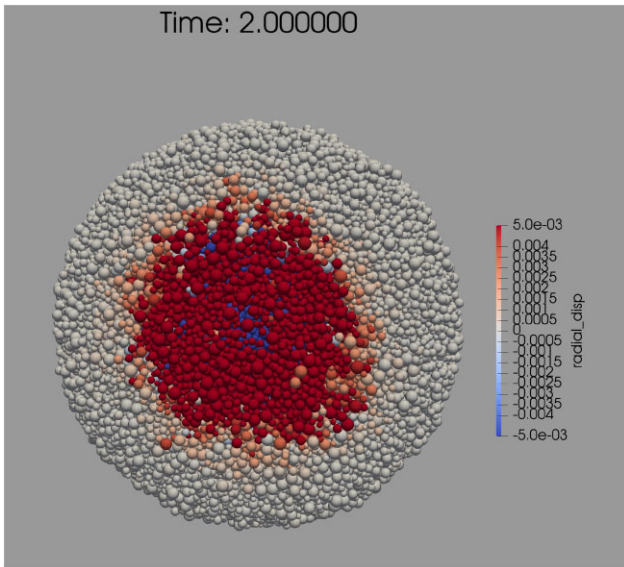
Figure 6. Radial displacement of surface particles. The colour bar is proportional to the value of the radial displacement, the projection of the displacement vector along the radius vector of the particle. Red colour corresponds to outward displacements (positive values), and blue colour corresponds to inward displacements (negative values).

$> 10^{-3}$ m s^{-1}. The rise time as a function of the maximum radial velocity is shown in Fig. 5.

We conclude that for particles up to $30°$ from the impact point, a velocity of $\sim 10^{-2}$ m s^{-1} is acquired in an interval of ~ 0.02 s. This corresponds to an acceleration of $a = \delta v / \delta t \sim 0.5$ m s^{-2}; which is related to the acceleration behaviour shown in Fig. 4*b* for particles at that distance.

Note that peak outward velocities up to 10^{-3} m s^{-1} are reached by particles up to $40°$ from the impact point. Also, peak outward accelerations well above the surface acceleration on Dimorphos are attained at distances over $60°$ from the impact point.

The propagation of the impact-induced waves produces radial displacements of 1 m size particles by over 1 mm at distances of 40–60° from the impact point (Fig. 6).

We observed that a spherical cap with an angle up to $60°$ from the impact point is affected by the propagation of the impact induced waves. This caps corresponds to an area $\sim 1/4$ of the total surface area of Dimorphos (i.e. $\sim 2 \times 10^4$ m^2).

The time-scale for the sudden increase in outward velocity is short, as it happens in most of the cases within the 1s after impact. 2 s after impact, very few particles are accelerated outwards, and the shaken area on the surface does not dramatically increase afterwards. This conclusion is evident in the videos of the supplementary material.

Finally, we want to note that we assumed a conservative estimate of the efficient coefficient for the transmission of kinetic energy from the impactor to the particles ($f_{ke} = 0.25$ per cent); however, there is a big uncertainty in this value. If the efficient coefficient is larger, the affected area should increase. Other free parameters that could affect the results are the assumed elastic constants and the impact geometry.

Therefore, we cannot rule out that the shaking mechanism could affect an even larger area. It could reach the hemisphere opposite to the impact point, all the way to the antipodal point.

3 LOFTING OF PARTICLES DUE TO SHAKING

3.1 The lofting mechanism

In this section, we analyse the arrival of the impact-induced seismic wave at points located far from the impact point, which produces a shaking effect on the ground. A preliminary analysis of this effect was done in Tancredi et al. (2012).

In the simulations described in the previous section, we considered m-size particles. We observed that mm outward displacements of surface particles in a time-scale of hundredth of a second can be produced by the impact-induced wave. Let's consider a regolith layer of small mm to cm-size particles on top of the large m-size ones. The shaking produced on the floor of the regolith layer will propagate up to the surface, and it will loft the small particles on the upper part of the layer. This is a well-known effect in common-day life. Take a can of fine powder like chocolate powder (cocoa) or flour. Strongly tap it from the bottom of the can, and you will see powder that is lofted from the surface. Due to the strong Earth's gravity, the dust particles immediately fall back. We call this the 'cocoa effect' (realized by G.T. when he was preparing breakfast for his kids).

This effect can also be observed in a more natural and geophysical environment. An earthquake produces strong shaking on the ground. If an earthquake happens in a desert and dusty area, a great amount of lofted dust is immediately produced after the arrival of the seismic waves due to shaking and landsliding. An example of this phenomena was observed after the magnitude 7.2 Mw earthquake occurred on 2010 April 4 in Northern Baja California (Mexico). Thick dust clouds were formed over the peaks of Sierra El Mayor immediately after, and they were recorded in a video by Sarah Klaus at 30 km south of Mexicali, on the main highway from Mexicali to San Felipe (https://www.youtube.com/watch?v=oeB-e3yBIho&t=21s/). The event was analyzed by Tancredi et al. (2010) and Barlow et al. (2015). Due to the small size of dust particles and the suspension in the atmosphere, the cloud persisted for several minutes, until it was dispersed by the wind. The propagation of the dust cloud was detected in satellite images.

The physics behind the 'cocoa effect' is out of the scope of this paper. We have been performing laboratory experiments as well as numerical simulations to understand it, and to find the relevant laws; e.g. the amount and velocity of lofted dust particles as a function of the floor's displacement. These results will be the matter of a
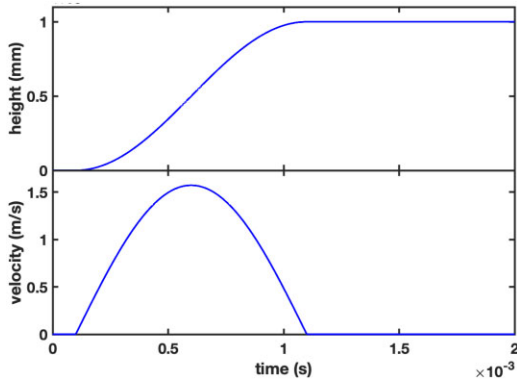
Figure 7. The displacement following a $\sin^2$ function, with variable amplitude and duration. The height of the floor h as a function of time t follows the equation: $h = A \sin^2\left(\frac{\pi}{2P}(t - dt_0)\right)$, where A is the maximum amplitude of the displacement ($A = 1$ mm), P is the duration ($P = 10^{-3}$ s), and dt_0 is the initial time separation ($dt_0 = 10^{-4}$ s). (a) The height of the floor as a function of time. (b) The velocity respect to the floor as a function of time.

future publication. In this paper, we just present some numerical simulations relevant to our problem.

Note that this mechanism is different from the crater and plume formation. In the formation of the crater, a volume many times the size of the projectile is excavated, and a fraction of it is ejected by forming a plume with a conical shape. The conical plume has a typical half-angle of 45°. The physics of the crater and the plume are represented by the point-source impact scaling laws by Housen & Holsapple ([2011](#)). From these laws, one can obtain the size of the crater, the amount of ejected material, and its velocity distribution, depending on parameters like the projectile mass and speed and the mechanical and gravity properties of the target.

The effect that we are discussing here, although related, is a different mechanism. The area affected by the impact can no longer be considered as a point source since it is many times larger than the crater. The lofted material is not confined in a conical plume, as it comes from a large area.

In order to analyse the relevance of the 'cocoa effect' for such problem, we performed some numerical simulations of the local effect on the surface using ESyS-Particle (it is not necessary to use ESyS-Gravity, because we do not need self-gravity among particles; a constant value for vertical gravity acceleration is enough).

Hereby, we describe the experimental setup. Consider a cubic box (4 cm size) filled with $\sim 300\,000$ particles, with radius between 0.2 and 0.5 mm, and material density of 3000 kg m^{-3}. One layer of particles was glued to the floor. The interaction among particles is viscoelastic Herztian with friction (see Tancredi et al. ([2012](#)) for the description of the model and parameters: Young modulus $Y = 10^{10}$ Pa, Poisson ratio $\nu = 0.3$, dissipative constant $A = 2e - 7$ s^{-1}, and dynamic friction parameter $\mu = 0.6$). The interaction of particles with the walls is elastic ($Y = 5^9$ Pa). The gravity acceleration is in the vertical direction, with $g = 10^{-3}$ m s^{-2}. A little after the beginning of the simulation, we apply to the floor a displacement following a $\sin^2$ function, with variable amplitude and duration, like the one shown in Fig. 7. The characteristic of the experiments are summarized below:

(i) A cubic box (4 cm size) filled with $\sim 300\,000$ particles
(ii) Particles radius: 0.2–0.5 mm; Density = 3000 kg m^{-3}
(iii) One layer of particles was glued to the floor
(iv) Interaction among particles: viscoelastic Herztian with friction ($Y = 10^{10}$ Pa). Elastic interaction with walls
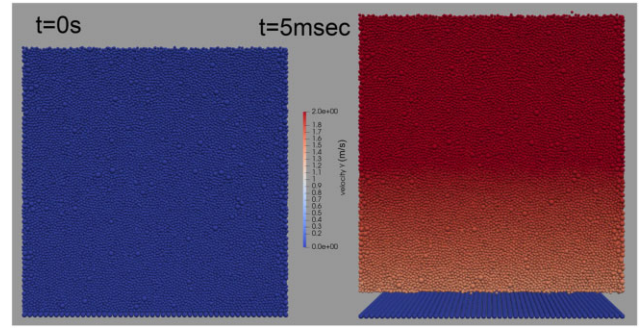
Figure 8. (a) The initial status of the box with particles at rest. After we apply the $\sin^2$ displacement to the floor, the particles glued with the floor move upwards, and they knock the particles above. This triggers particle motion upwards, but due to mutual collisions, there are differential velocity displacements. The particles on the upper layer move faster than the lower ones, as can be seen in Fig. (b) at 5 milliseconds after the start.

(v) Gravity: $g = 10^{-3}$ m s^{-2}
(vi) A displacement of the floor following $\sin^2$ function, with variable amplitude.

In Fig. [8a](#), we present the initial status of the box with particles at rest. After we apply the $\sin^2$ displacement to the floor, the particles glued with the floor move upwards, and they knock the particles above. This triggers particle motion upwards, but due to mutual collisions, there are differential velocity displacements. The particles on the upper layer move faster than the lower ones, as can be seen in Fig. [8b](#), at 5 milliseconds after the start. A vertical velocity gradient can be observed. To show the differences between the upper and lower layers, we compute the median height and velocities of the bottom 10 per cent quantile and the top 90 per cent quantile of particles ordered by height. The evolution of these parameters is shown in Fig. [9](#). We present results from two experiments of $\sin^2$ displacement, they have the same amplitude of displacement, 10^{-3} m, but different half-duration: 10^{-2} s and 10^{-3} s, respectively. In both cases, the displacement starts at 2×10^{-3} s after the simulation starts, like the one in Fig. [7](#). In Fig. [9](#), we observe that the bottom layer starts to move upwards, and afterwards the upper layer starts moving. When the pulse is fast (i.e. half-duration of 10^{-3} s), the difference between the velocity of the upper to the lower layer is wider; but, if the pulse is slow, the upper layer goes along the displacement of the lower layer.

3.2 Summary of results of the shaking process

The displacement of the floor of a regolith layer of mm-size particles, in a hundredth of a second (or faster), produces the lofting of the upper part of the layer, with particle ejection velocities comparable to the escape velocity of Dimorphos (~ 0.1 m s^{-1}).

Since, in Section [2.3](#), we observed that this kind of displacement would take place in a large area of the impacted hemisphere, we conclude that the lofted material will come from large distances from the impact point. Unlike the plume cone, in which dust particles are generally moving radially from the impact point, the lofted material due to shaking will be distributed nearly in an isotropic way.

Let's consider there is a 10 cm regolith layer covering the surface of Dimorphos, similar to the layers observed in Eros (Richardson et al. [2005](#)) and Itokawa (Michel et al. [2009](#)). Based on the results in Section [2.3](#), we estimate the area affected by the shaking mechanism of at least $\sim 1/4$ of the total surface area of Dimorphos (i.e. $\sim 2 \times 10^4$
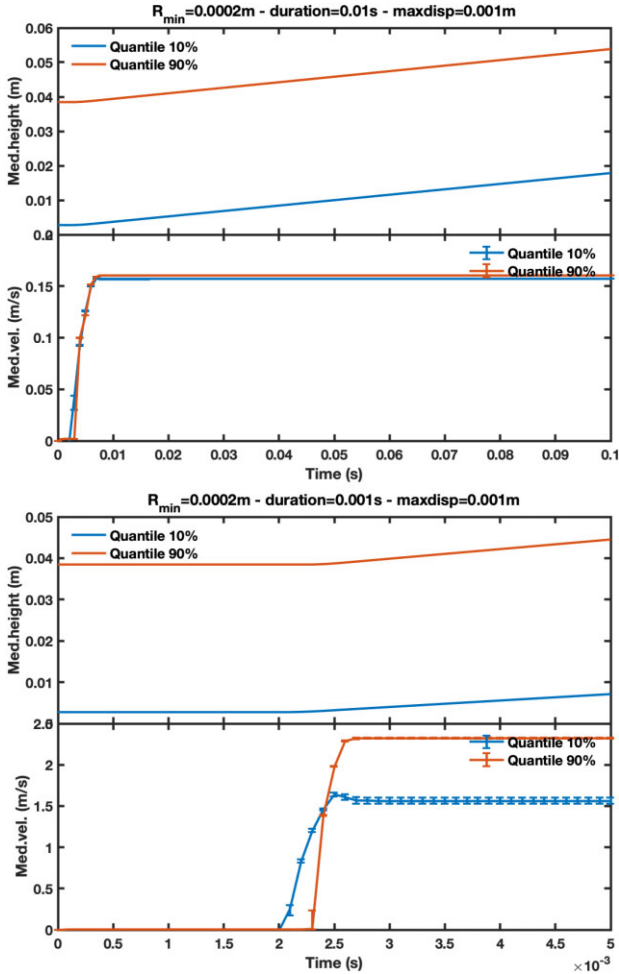
Figure 9. The median height and velocities of the bottom 10 per cent quantile and the top 90 per cent quantile of particles ordered by height. We present results from two experiments of $\sin^2$ displacement; they have the same amplitude of displacement, 10^{-3} m, but different half-duration: (a) 10^{-2} s and (b) 10^{-3} s, respectively.

m^2). Assuming a particle density of 3000 kg m^{-3}, and macroscopic porosity of 50 per cent, we get a total mass of the affected regolith layer of $\sim 3 \times 10^6$ kg. This amount of mass in mm to cm-size dust particles could be ejected at velocities comparable to the escape velocity.

Using the point-source impact scaling laws by Housen & Holsapple (2011), both Cheng et al. (2022), Moreno et al. (2022) estimated a total ejected mass due to crater formation on Dimorphos of $\sim 4 - 5 \times 10^6$ kg (at velocities above $v_{\mathrm{esc,\,Dim}}$), which is comparable to our value of lofted material. Using *SPH* simulations, (Ferrari et al. 2022) made an estimate of the total ejected mass with velocities above the $v_{\mathrm{esc,\,Dim}}$ of $\sim 5 \times 10^3 \times$ the mass of the impactor, i.e. $\sim 2.8 \times 10^6$ kg, a similar value to the previous ones. The main difference is that the lofted material would have ejection velocities just above the escape velocities, while the material in the plume will move much faster. This difference has important implications for the observability of the ejecta cloud, as we will show next.

Obviously, there are huge uncertainties in the above estimates, because we do not know the surface structure of Dimorphos, and we only have a rough estimate of the affected area, which depends, as was mentioned in Section 2.3, on many free parameters of simulations.

We just want to emphasize that the 'cocoa effect' could be a relevant phenomena that cannot be disregarded.

4 EJECTION OF PARTICLES AND PREDICTIONS FOR THE OBSERVATIONS

The evolution of the particles ejected from Dimorphos's surface at different speeds was already studied by our group, and some results were presented in Moreno et al. (2022).

Two sets of observations of the aftermath of the DART experiment will be performed: (i) The observation of evolution of the impact itself, in the first few minutes during the LICIACube fly-by, with enough resolution to closely observe Dimorphos' and Didymos' surfaces; (ii) The long-term monitoring from distant telescopes (from ground and space) of the dust coma and tail generated by the impact. We will analyse the detectability of the ejecta in these two sets of observations.

The evolution of the dust cloud generated by the impact has a strong dependence on the ejection speeds. The ejected material can be broadly classified into three different regimes: the very-high-speed ejecta, with velocities from the surface over $v > 10$ m s^{-1}; the high-speed ejecta, with $1 < v < 10$ m s^{-1}, and the low-speed ejecta, with $v < 1$ m s^{-1}.

The very-high and high-speed ejecta are generated in the cratering event and from the crater area, as well as are ejected within the conical plume. The very-high speed ejecta will be observed by LICIACube in the first seconds after the impact; since, by the time of close approach ($t_{cl} = +167$ s after impact), the very-high speed ejecta will overtake Didymos. If these very-high speed ejecta ever exist, and depending on the geometry of the actual impact and the orientation of the plume with respect to Didymos, some dust particles could travel directly towards Didymos, producing some observable impact flash on the surface, similar to the impact flashes observed on the Earth's Moon surface; but it might be difficult to detect them due to the rate of image acquisition by LICIACube.

The high-speed ejecta will be seen by LICIACube slowly moving within the conical plume during the approaching and the receding phases. At t_{cl}, most of the high-speed material will still be within the Didymos system, at distances of a few hundreds m up to slightly over 1 km from Dimorphos.

The visibility of the ejecta plume was discussed in detail by Cheng et al. (2020 and 2022). Hereby, we analyse the evolution and observability of the low-speed ejecta.

4.1 The first seconds after impact and the observations by LICIACube

Part of the low-speed ejecta will be formed in the cratering event and they will move within the conical plume. In addition, as we propose in the previous sections, the propagation of the impact-induced seismic wave will produce a strong shaking in a large area surrounding the impact point. Such a shaking will trigger the occurrence of the 'cocoa effect': the lofting at very low velocity of fine particles coming from a large surface area. Lofted particles will move away from Dimorphos surface at speeds comparable to the escape speed ($v_{\mathrm{esc,\,Dim}} \approx 0.089$ m s^{-1}). Let's recall that the existence of low-speed ejecta is supported by observations of long-lasting dust tails in Active Asteroids.

Particles moving with velocities $v < v_{\mathrm{esc,\,Dim}}$ will fall back after suborbital flight that could last minutes. Therefore, during the LICIACube fly-by, there will be dust material just above the surface. Particles moving upwards with $v_{\mathrm{esc,\,Dim}} < v < v_{\mathrm{esc,\,Sys}}$ will
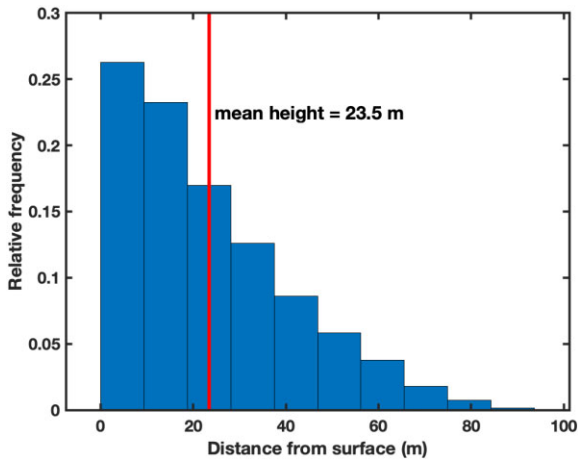
Figure 10. A histogram of the relative frequency of the distances from Dimorphos' surface of the 50 000 particles at + 100 s after impact. The distances were calculated with the model described in the text. The vertical red line corresponds to the mean height of 23.5 m.

be governed by the dynamics of the binary system. The seismic wave reaches a large fraction of the entire Dimorphos body in less than 2*s*, and they immediately produce shaking of the floor and lofting of particles. At t_{cl} lofted material at velocities a few times $v_{esc, Dim}$ will be a few m, up to a few tens of m, above the surface of the impacted hemisphere. If the impact-induced seismic wave ever reaches the antipodal hemisphere, lofted material could be observed over the entire surface.

The Hill's radius of Dimorphos in the binary system is ∼171 m, roughly 2× Dimorphos radius. Particles leaving Dimorphos surface at ejection velocities a few times $v_{esc, Dim}$ will move inside Dimorphos Hill's radius in the first tens of seconds after the impact. Therefore, to study the early evolution of the ejecta cloud at low speed, we consider only the motion of particles under the influence of Dimorphos gravity field. Let's consider a Monte Carlo model for a set of particles leaving Dimorphos surface. Ejection velocities are in a range spanning from the circular velocity at the surface ($v_{circ, Dim} = 0.063$ m s^{-1}) up to $10 \times v_{esc, Dim}$, with a triangular shaped distribution. The lower limit of speed is such that particles can rise from the surface. Velocity vectors are pointing outwards with an isotropic distribution in the outgoing hemisphere. Particles with velocities v from $v_{circ, Dim}$ up to $v_{esc, Dim}$ will get elliptical orbits, and lately fall back to Dimorphos. Particles with velocities $v > v_{esc, Dim}$ will move in hyperbolic orbits away from Dimorphos, asymptotically approaching the velocity at infinity given by: $U = \sqrt{v^2 - v_{esc,Dim}^2}$. By solving the Kepler's equations, we compute the distance of the particles from Dimorphos' surface at a given time after impact (e.g. + 100 s). With the above range of ejection velocities, particles will be at 100 s after impact at heights above the surface from 0 up to 90 m (Fig. 10), with a mean value of 23.5 m. At the time of closest approach ($t_{cl} = +167$ s), the mean height of the cloud would be 42 m.

Such dust particles at low height from the surface and spread over a large area would obscure the visibility of Dimorphos surface, producing a hazy effect, similar to the picture taken after the Mexicali earthquake.

A precise estimate of the effect of this dust cloud on the observability from LICIACube is a great challenge, due to the several uncertainties in the model, like the total amount of ejected mass, the size range and size distribution of particles, the extent of the area affected by the shaking mechanism, the velocity distribution of

particles, among others. Just to have an idea of the relevance of this effect, let's assume the following model: (i) a layer of particles above Dimorphos' surface with a given height h, following the results of the ejection model described above; (ii) a total ejected mass in low-speed ejecta of $M_{ej} \sim 3 \times 10^6$ kg; (iii) particles in a size range from 1 mm to 1 cm; with a power-law size distribution similar to the one observed on the surface of asteroid Itokawa, with a differential mass index of $\beta = -3.2$ (Tancredi, Roland & Bruzzone 2015); (iv) particle's density $\rho = 2170$ kg m^{-3}.

The amount by which each particle of radius r reduces the radiant beam I_0 is $\pi r^2 k_e I_0$, where k_e is the extinction coefficient. Adding the contribution of the cloud of particles, we obtain the following expression for the optical depth:

$$\tau = \pi h \int_0^\infty k_e(r) r^2 n(r) \mathrm{d}r \quad (5)$$

where $n(r)$ is the number density distribution of particles. $n(r) = f(r)/V$, where $f(r)$ is the size distribution of particles, and V is the volume of the cloud over the impacted hemisphere: $V = \frac{2}{3}\pi \left((r_{Dim} + h)^3 - r_{Dim}^3\right)$. We are assuming that the ejected particles are coming mainly from the impacted hemisphere, which happens to be the hemisphere seen by LICIACube in its approaching phase.

In this model, we are assuming that there is no mutual shadowing of the particles. Particles scatter light individually and no effect of multiple scattering is considered.

We assume a mass distribution:

$$f(m) = \begin{cases} Cm^\beta, & \text{if } m \in [a, b]. \\ 0, & \text{otherwise.} \end{cases} \quad (6)$$

The parameter C can be obtained from the equation of the total mass of the cloud:

$$M = \int_0^\infty m f(m) \mathrm{d}m = \int_a^b m C m^\beta \mathrm{d}m = \frac{C}{(\beta + 2)} b^{\beta+2} - a^{\beta+2}. \quad (7)$$

We then obtain:

$$C = \frac{M(\beta + 2)}{b^{\beta+2} - a^{\beta+2}}. \quad (8)$$

Replacing in equation 5 $f(r)\mathrm{d}r = f(m)\mathrm{d}m$, and integrating in the range $[a, b]$, we obtain:

$$\tau = 2\pi \frac{h}{V} \left(\frac{3}{4\pi\rho}\right)^{\frac{2}{3}} \frac{C}{\beta + \frac{5}{3}} \left(b^{\beta+\frac{5}{3}} - a^{\beta+\frac{5}{3}}\right). \quad (9)$$

Considering that the mean height of the cloud at 100 s after impact is $h = 23$ m, we obtain an optical depth over the surface of Dimorphos of $\tau \sim 21$. Only $\exp(-\tau) = 7 \times 10^{-10}$ of the radiation coming from Dimorphos surface would be observed by LICIACube. At the time of the closest approach ($t_{cl} = +167$ s), the optical depth will reduce to $\tau \sim 17$, and the total brightness reduction will be by a factor of 3×10^{-8}.

If the amount of dust released by the shaking mechanism is reduced by a factor of 10 with respect to the previously assumed value (i.e. $M_{ej} \sim 3 \times 10^5$), the optical depth at $t = +100$ s will be reduced by a similar factor to $\tau \sim 2$ and the brightness reduction factor to ∼0.12; and at closest approach, the numbers are $\tau \sim 1.7$ and the brightness reduction factor ∼0.18.

In any of these scenarios, the radiation coming from Dimorphos surface will be considerably absorbed and scattered by the dust cloud. In addition to the absorption effect, there would be a strong blurring effect that would make it difficult to detect surface features. It would not be possible to clearly observe Dimorphos' surface, as it happened with the hills behind the dust cloud in the Mexicali earthquake.
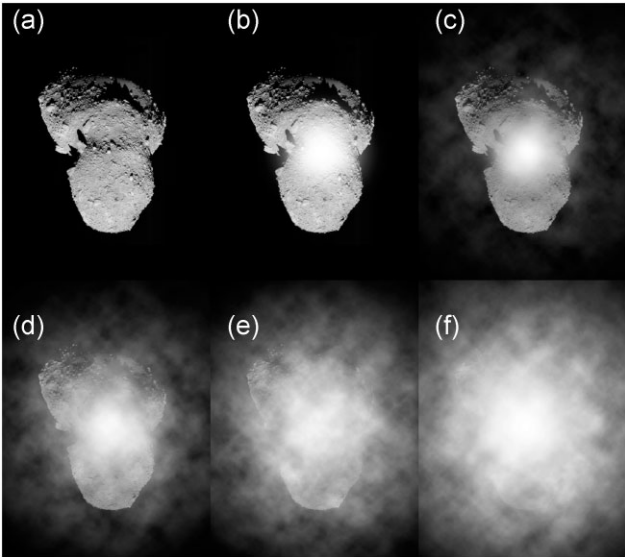
Figure 11. A set of artistic renders of the dust cloud, using an image of Itokawa taken by Hayabusa as a model. We assume that LICIACube's camera is pointing directly to the impact point. The sequence corresponds to an image at ∼100 s after impact and alternative scenarios depending on the amount of material ejected at low speeds. The sequence starts with (a) the bare body, (b) the brightening and the conical plume seen from the axis direction, with negligible contribution from the low-speed ejecta, and (c)–(f) an image sequence with an increasing contribution of low-speed ejecta from a wide area of the impacted hemisphere.

As an illustration of the different scenarios that LICIACube could face, we produce a sequence of artist's render of the dust cloud using an image of Itokawa taken by Hayabusa as a model (Fig. 11). We assume that LICIACube's camera is pointing directly to the impact point. The sequence corresponds to a snapshot taken at ∼100 s after impact and alternative scenarios depending on the amount of material ejected at low speeds. The sequence starts with (a) the bare body, (b) the brightening and the conical plume seen from the direction of the cone axis, with negligible contribution from the low-speed ejecta, and (c)–(f) an image sequence with an increasing contribution of low-velocity ejecta from a wide area of the impacted hemisphere.

This issue will not affect the observation of Didymos from LICIACube, unless a very particular configuration of a quasi-mutual eclipse happens, since the dust cloud will be very close to Dimorphos' surface.

4.2 The formation of the coma and the tail, and the observations from distant telescopes

In our previous work (Moreno et al. 2022), we studied the evolution of the brightness of the coma and the tail as a function of ejection speed. We performed simulations with a wide range of possible ejection velocities, from Dimorphos escape velocity of 0.09 m s^{-1} up to 800 m s^{-1}. A nominal value of the total ejected mass of 5×10^6 kg was used for the calculations; although, we also presented some results with a larger amount of ejected mass.

A Monte Carlo approach was used to model the evolution of μm to cm dust particles under the gravity forces of Dimorphos, Didymos, and the Sun and SRP, the only non-gravitational force acting on particles that we considered in the model. The Poynting–Robertson drag on those particles is only important in very long-term dynamics, and was therefore neglected. Particles follow a differential power-law
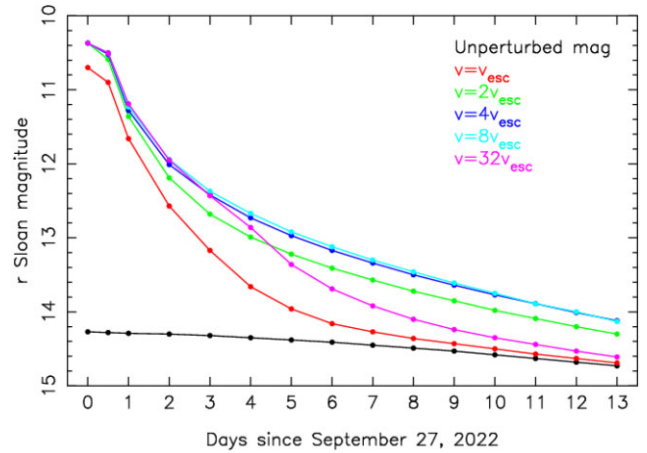
Figure 12. Calculated *r*-Sloan magnitudes as a function of date and ejection velocities, for slow ejection speeds, compared to the unperturbed system magnitude. See Moreno et al. (2022) for the details of the model.

size distribution with exponent -3.5 in the range from 1 μm to 1 cm. We propagated the orbits of ejected particles by integrating their equation of motion, and the results were used to study the evolution of the coma and the tail brightness.

Note that in this model, we considered particles down to 1 μm in size. Those very small particles will be strongly affected by the SRP, even at the early stages of ejection. For example, a 1 μm particle released from the surface at 0.1 m s^{-1} will be accelerated up to a velocity of 5 m s^{-1}, 2 h after the impact, while a 100 μm particle will have a velocity of 0.2 m s^{-1} after the same time. Therefore, the smallest particles will disperse quickly, and their contribution to the coma and the long-lasting tail will be small, as it has been observed in the modelling of Active Asteroids (Moreno et al. 2021).

The model computed the asteroid tail surface brightness and the integrated brightness of the coma at a given date as seen from the Earth. The nucleus brightness of Didymos was also included in the simulated images.

For low-speed ejecta, up to a several times Dimorphos escape velocity, Moreno et al. (2022) predicted an increase of brightness of ∼3 mag right after the impact, and decay to pre-impact levels some 10 d after (see fig. 7 of Moreno et al. 2022). However, if most of the ejecta is released at speeds of the order of $\geq$100 m s^{-1}, the observability of the event would reduce to a very short time span, of the order of 1 day or shorter.

To discuss in more detail the effects of the low-speed ejecta, we extend fig. 7 of Moreno et al. (2022) to include several curves for the low-speed cases (Fig. 12), and extending the calculations to show results at still shorter times relative to the impact time. In this new plot, the first data points are at September 27 00:00 UT, i.e. only 46 min after impact. During the first few hours after impact, the increase of brightness relative to the unperturbed system could reach up to ∼4 mag for ejecta speeds between 2 and 32 × $v_{\rm esc,Dim}$.

Let's consider the case of particles with ejection speeds 4 × $v_{\rm esc}$. Immediately after the impact, the object will increase its brightness by ∼4 mag with respect to the bare Didymos system; 5 d after the impact, the integrated magnitude of the coma will still be 1.4 mag brighter than the nucleus; and 10 d after the impact, the difference will be 0.8 mag. In the latter case, the total flux will be twice the nucleus flux; therefore, half of the total brightness would come from the bare system and the other half from the surrounding coma. According to

the previous studies (Pravec et al. 2006), the magnitude drop due to mutual events is ~ 0.1 mag. Because of the large contribution of the dust coma to the total brightness in the first few days after impact, the small dips associated with mutual events would be masked and difficult to detect.

The comma flux scales approximately with the total particle area and, consequently, with the total mass ejected. Therefore, a factor of $10\times$ increase (decrease) on the amount of ejected mass would produce a $\sim 2.5\log_{10}10 = 2.5$ mag upward (downward) shift of the curves in Fig. 12 (see fig. 9 of Moreno et al. 2022).

Monitoring the evolution of total brightness in the first 2–3 d after impact can be used to estimate when the contribution of the coma will be negligible. The observed magnitudes can be located in the plot of Fig. 12, and the curve that best matches observations can be used to extrapolate for later days.

5 CONCLUSIONS AND DISCUSSION

The DART impact experiment on the Didymos satellite, Dimorphos will take place on 2022 September 26 at 23:14 UT. The impact will produce a crater and ejected material at high-speed in a conical plume. In addition, impact generated seismic waves will propagate inside Dimorphos. The attenuation of those waves depends on the mechanical properties of the material, which are largely unknown. Using some realistic mechanical properties of rocky material in two different types of DEM simulations, we studied the propagation of the waves at a large distance from the impact point on the surface. We worked out that, from a few tenths of a second after impact up to 2 s, the particles located several tens of degrees from the impact point may be shaken due to the incoming seismic wave. If a thin regolith layer located on the surface is shaken, the top of the layer can be ejected at velocities comparable to the escape velocity from the Dimorphos surface. We call this phenomena the 'cocoa effect'. We estimate that an area on the order of at least 1/4 of the total surface of Dimorphos could be shaken and several thousand tons of dust could be released at low velocities (less than 1 m s^{-1}). The motion of the ejected dust particles will be affected by the gravitational forces of mainly Dimorphos, Didymos, and the Sun, as well as the SRP.

As a consequence of such sequence of events, we anticipate the following potentially observable effects: (i) generation of a cloud of small particles that would produce a hazy or fuzzy appearance of Dimorphos surface, detectable by LICIACube; (ii) brightness increases of the binary system due to enhancement of the cross-section produced by the cloud of particles; (iii) generation of a dust trail, similar to those observed in Active Asteroids, which can last several weeks after impact.

A prediction of the observability of these effects strongly depends on the amount and size distribution of ejected particles, which are largely unknown. The monitoring of the Didymos system in the hours and days after the impact can be used to discuss the relevance of the different ejection mechanisms; and, by an inversion analysis, estimates of some elastic and structural parameters of Dimorphos can be obtained.

It is worth saying that the presence of low-speed ejecta might not have relevant consequences for the key objective of the DART mission, i.e. get an estimate of the efficiency of linear momentum transfer from the projectile to the target. Assuming a total ejected mass at low speed of $\sim 3 \times 10^6$ kg, the kinetic energy carried by the dust cloud at velocities of $\sim 0.1 \text{ m s}^{-1}$ would be $< 10^{-4} \times$ the kinetic energy of the DART spacecraft. The sum of the modulus of the linear momentum of the released particles would be $0.1\times$ the linear momentum provided by the DART spacecraft. However, the net effect depends on the vector addition of the individual linear momenta of particles, and therefore such effect will be largely less than 0.1.

Finally, we emphasize that the DART experiment can be considered as the production of an artificial Active Asteroid, with an extensive set of follow-up activities at the moment of impact and beyond. Therefore, the DART experiment will also provide – as an additional side product – useful information for understanding the physics of the generation of Active Asteroids.

DATA AVAILABILITY

The plots included in this article were generated with data coming out of the simulations. We can provide the interested readers with the initial conditions of the simulations in more detail than the ones described in the text, as well as the outcomes of the simulations. Please contact the corresponding author.

REFERENCES

Abe S., Place D., Mora P., 2004, Pure Appl. Geophys., 161, 2265
Barlow J., Barisin I., Rosser N., Petley D., Densmore A., Wright T., 2015, Geomorphology, 230, 138
Cheng A. F., Raducan S. D., Fahnestock E. G., Dotto E., Corte V. D., Stickle A. M., 2022, Planet. Sci. J., 3, 131
Cheng A. F., Stickle A. M., Fahnestock E. G., Dotto E., Della Corte V., Chabot N. L., Rivkin A. S., 2020, Icarus, 352, 113989
Fahnestock E. G. et al., 2022, Planet. Sci. J., 3, 206
Ferrari F., Raducan S. D., Soldini S., Jutzi M., 2022, Planet. Sci. J., 3, 177
Frascarelli D., Nesmachnow S., Tancredi G., 2014, Computer, 47, 34
Gallot T., Tancredi G., Ginares A., 2019, Acoust. Soc. Am. J., 145, 1903
Goddard J. D., 1990, Proc. R. Soc. London. Series A: Math. Phys. Sci., 430, 105
Hainaut O. R. et al., 2019, A&A, 628, A48
Housen K. R., Holsapple K. A., 2011, Icarus, 211, 856
Jewitt D., Hsieh H. H., 2022, in Meech K., Meech M., eds, Comets III. University of Arizona Press, Tucson, AZ
Jewitt D., Weaver H., Mutchler M., Larson S., Agarwal J., 2011, ApJ, 733, L4
Michel P., O'Brien D. P., Abe S., Hirata N., 2009, Icarus, 200, 503
Moreno F. et al., 2011, ApJ, 738, 130
Moreno F., Campo Bagatin A., Tancredi G., Liu P.-Y., Domínguez B., 2022, MNRAS, 515, 2178
Moreno F., Licandro J., Cabrera-Lavers A., Morate D., Guirado D., 2021, MNRAS, 506, 1733
Nesmachnow S., Rocchetti N., Tancredi G., 2019, in 2019 Winter Simulation Conference (WSC), Large-Scale Multithreading Self-Gravity Simulations for Astronomical Agglomerates. p. 3243

Pravec P. et al., 2006, Icarus, 181, 63

Raducan S. D., Davison T. M., Collins G. S., 2022, Icarus, 374, 114793

Richardson D. C., Quinn T., Stadel J., Lake G., 2000, Icarus, 143, 45

Richardson J. E., Melosh H. J., Greenberg R. J., O'Brien D. P., 2005, Icarus, 179, 325

Rivkin A. S. et al., 2021, Planet. Sci. J., 2, 173

Rocchetti N., Nesmachnow S., Tancredi G., 2018, in Meneses E., Castro H., Barrios Hernández C., Ramos-Pollan R., eds, Communications in Computer and Information Science, Vol 979, High Performance Computing. CARLA 2018. Springer, Cham, p. 141

Rocchetti N., Nesmachnow S., Tancredi G., 2021, High-Performance Computing Simulations of Self-gravity in Astronomical Agglomerates. SIMULATION

Schwartz S. R., Richardson D. C., Michel P., 2012, Granular Matter, 14, 363

Tancredi G., 2014, Icarus, 234, 66

Tancredi G., Maciel A., Heredia L., Richeri P., Nesmachnow S., 2012, MNRAS, 420, 3368

Tancredi G., Roland S., Bruzzone S., 2015, Icarus, 247, 279

Tancredi G., Sanchez Bettucci L., Maciel A., Elgue I., 2010, in Meeting of the Americas of the American Geophysical Union. p. U41A–20

Walker J. D., Chocron S., Durda D. D., Grosch D. J., Movshovitz N., Richardson D. C., Asphaug E., 2013, Int. J. Impact Eng., 56, 12

Walsh K. J., Richardson D. C., Michel P., 2008, Nature, 454, 188

SUPPORTING INFORMATION

We present videos of the evolution for 10 s after impact of radial velocity in a cross section through the centre of the target and the impact point, and from a viewpoint located above the impact point. Supplementary data are available at *MNRAS* online.

slice_radial_vel.avi
surface_radial_vel.avi

Please note: Oxford University Press is not responsible for the content or functionality of any supporting materials supplied by the authors. Any queries (other than missing material) should be directed to the corresponding author for the article.

This paper has been typeset from a TEX/LATEX file prepared by the author.